

Article

Bimetal-Initiated Concerted Zn Regulation Enabling Highly Stable Aqueous Zn-Ion Batteries

Hong Yin ¹, Yuliang Liu ¹, Yifeng Zhu ¹, Fengxiang Ye ², Guangliang Xu ^{1,*}, Mengfang Lin ^{2,*} and Wenbin Kang ^{1,*}

¹ State Key Laboratory of Environmentally Friendly Energy Materials, School of Materials and Chemistry, Center of Analysis and Characterization, Southwest University of Science and Technology, Mianyang 621010, China; yinhong@mails.swust.edu.cn (H.Y.); liuyuliang@swust.edu.cn (Y.L.); zhuyifeng@mails.swust.edu.cn (Y.Z.)

² Department of Materials Engineering, Ming Chi University of Technology, New Taipei City 24301, Taiwan; u09187035@mail2.mcut.edu.tw

* Correspondence: xuguangliang@swust.edu.cn (G.X.); mflin@mail.mcut.edu.tw (M.L.); wenbin.kang@swust.edu.cn (W.K.)

Abstract: Aqueous zinc ion batteries are highly sought after for the next generation of sustainable energy storage systems. However, their development is significantly impeded by the presence of undesired zinc dendrites, which greatly reduce their cycle life. It is well-received that surface passivation by introducing foreign metals represents a compelling measure to enhance the stability of Zn anodes. Nevertheless, the vast potential of effecting concerted interplay between multiple metal elements for enhanced overall performance in Zn ion batteries remains elusive, due to the overwhelming challenge in creating uniform textures from hetero-units and understanding the mechanism underlying the synergistic performance gain. In this work, an innovative bimetallic overlaying strategy is proposed that renders possible the synergy between AgZn₃ and CuZn₅ in effecting uniform Zn deposition in a laterally confined and compact manner. The seeded growth of Zn on the bimetal-modulated interface effectively reduces the nucleation potential barrier, yielding a low nucleation overpotential (25 mV). In full cell testing with a commercial MnO₂ applied as the cathode, superb cycling stability, surpassing the results reported in previous works, is achieved. The cell delivers an outstanding remaining capacity of 215 mA h g⁻¹ after 300 cycles with almost no capacity degradation observed. The simple and highly efficient bimetal design, which synergizes the strengths of distinct metals, has the potential to drive innovations in the development of multicomponent aqueous Zn batteries with exceptional performance.



Citation: Yin, H.; Liu, Y.; Zhu, Y.; Ye, F.; Xu, G.; Lin, M.; Kang, W. Bimetal-Initiated Concerted Zn Regulation Enabling Highly Stable Aqueous Zn-Ion Batteries. *Batteries* **2024**, *10*, 70. <https://doi.org/10.3390/batteries10030070>

Academic Editors: A. Robert Armstrong, Yuanhua Xiao, Ling Wu, Xianwen Wu and Yiping Tang

Received: 8 December 2023

Revised: 22 January 2024

Accepted: 8 February 2024

Published: 20 February 2024



Copyright: © 2024 by the authors. Licensee MDPI, Basel, Switzerland. This article is an open access article distributed under the terms and conditions of the Creative Commons Attribution (CC BY) license (<https://creativecommons.org/licenses/by/4.0/>).

1. Introduction

Compared to the high cost and safety issue of lithium-ion batteries (LIBs), zinc ion batteries (ZIBs) with aqueous zinc salt electrolytes are highly desired for the next-generation green energy storage systems owing to their intrinsic safety, low-cost, and eco-friendliness [1–3]. Meanwhile, a Zn anode with high theoretical capacity (820 mA h g⁻¹) and low redox potential (−0.76 V versus SHE) enables ZIBs to deliver relatively high theoretical energy densities [4,5]. Therefore, ZIBs have been investigated extensively and great progress has been made in recent decades [6–8]. However, the zinc dendrite growth and hydrogen evolution reaction (HER) on the Zn anode during charge/discharge processes greatly compromise the cycling stability and coulombic efficiency of ZIBs [9].

Particularly, zinc dendrite growth and corrosion on the surface of zinc foil disc are the main issues that need to be resolved urgently [10–12]. It has been revealed that zinc prefers to deposit on the sites with lower surface energy during the zinc deposition process, which leads to the formation of needle-like dendrites [13]. Consequently, there is a higher electric field at the tip of the zinc dendrite due to the modulation of the electric field on

the uneven surface of the zinc foil disc [14]. As shown in Figure 1a, zinc dendrites are gradually extended towards the cathode materials and eventually lead to a short-circuit. Meanwhile, corrosion will produce by-products and hydrogen on the surface of Zn. This increases the internal resistance and bloats the battery, eventually leading to battery failure. To effectively inhibit the growth of dendrite and corrosion on zinc, a variety of strategies have been suggested to enhance the performance of Zn anodes, including the application of anode protective coatings [15–17], the enhancement of anode surfaces through in situ recombination and structural optimization [18,19], and the integration of electrolyte additives [20–22]. Specifically, the application of protective coatings is a straightforward and effective approach to mitigate the challenges faced by Zn anodes. For instance, coatings composed of polymers with a three-dimensional or porous structure and hydrophilic zinc functional group effectively entraps water molecules to minimize side reactions. Additionally, they regulate uniform Zn^{2+} flux through a confinement effect, thereby enhancing the battery's cycling stability [23]. Nevertheless, the complexity of the synthesis process limits its practical implementation. Another approach involves the use of inorganic compound protective layers, such as CaF_2 [16], which exhibit corrosion resistance and low polarization. These properties facilitate Zn^{2+} diffusion, suppress hydrogen evolution, and reduce the electrode's interfacial impedance. Such layers can be efficiently designed to control the nucleation, growth, and reversibility of zinc metal. However, during the stripping/plating process, particularly after prolonged cycling at high current densities, these inorganic layers, characterized by their low toughness and poor adhesion to the zinc foil substrate, are prone to cracking and damage due to the volumetric changes of the zinc anode. In contrast, alloys developed from the introduction of foreign metals that demonstrate high toughness and strong affinity for zinc foil substrates show promise in promoting uniform zinc deposition and accommodating significant volume changes during cycling [24]. Such surface passivation by foreign metals has been proven particularly effective in reducing the nucleation overpotential and polarization voltage of Zn, thus multiplying the nucleation sites and facilitating the uniform deposition of Zn on metal current collectors with favorable binding energies [25]. Typical choices of metal such as Cu [26,27], Ag [28], Ni [29] and Sn et al. [30] have been reported. Due to the distinct physiochemical properties of different metals, they exhibit unique strengths in terms of binding energy, surface free energy, solubility in Zn, crystal structures, and orientation, etc. However, existing works primarily focus on constructing alloy protective layers using single metals. The immense potential of synergistic interplay between metals has thus been overlooked due to the challenges in achieving uniform textures from heterogeneous building blocks and comprehending the underlying mechanism that leads to enhanced performance [31].

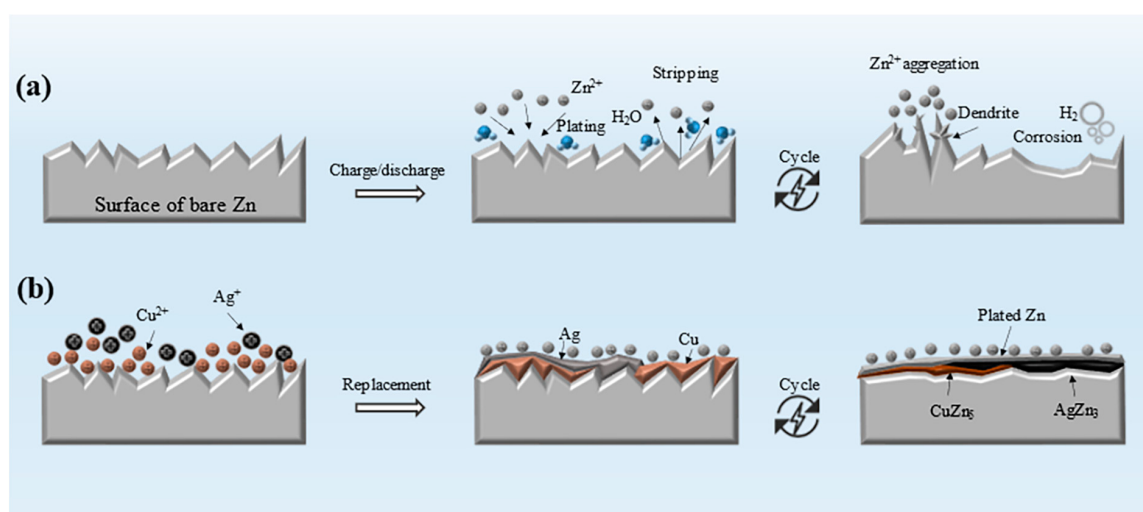


Figure 1. Schematics for (a) reactions occurring on the bare zinc anode during cycling and (b) on the bimetal modified surface.

In this work, Zn anode overlaid with protective bimetals has been realized. The negative Gibbs free energy change prompts the spontaneous formation of CuZn₅ and AgZn₃ alloys during the seeded growth of Zn. It is found that the highly matching crystal structure between AgZn₃ and Zn, with predominant (002) planes in AgZn₃, facilitates the epitaxial growth of Zn. Additionally, the surrounding CuZn₅, with its strong binding capability, effectively anchors Zn²⁺ and suppresses its vertical diffusion. The concerted interplay among the benefits contributed by the bimetals culminates in significantly reduced polarization and highly regulated Zn deposition, bringing about dendrite-free ZIB with exceptional cycling stability.

2. Materials and Methods

2.1. Preparation of the Modified Anodes

The Ag@Zn anode was prepared by using metal substitution reaction. Typically, zinc foil of 0.1 mm thickness was cut into 14 mm diameter disc. Then, the zinc foil wafer was immersed into 0.2 M HCl for 3 min to remove the impurities, and oxides in the zinc foil surface, and cleaned with deionized water and anhydrous ethanol three times. After drying at 60 °C under vacuum for 2 h, the zinc foil wafer was soaked in 20 mL anhydrous ethanol solution of 0.01 M AgNO₃ for 20 min. Finally, the Ag@Zn anode was obtained after drying at 60 °C under vacuum for 10 h. The Cu@Zn anode was prepared under the same conditions except that 0.01 M AgNO₃ was replaced by 0.1 M Cu(NO₃)₂. And the preparation of Ag-Cu@Zn anode was just realized by adding 0.01 M AgNO₃ and 0.1 M Cu(NO₃)₂ at same time at the corresponding step.

2.2. Material Characterization

The microscopic morphology and elemental composition and distribution of the electrodes were determined by field emission scanning electron microscopy (SEM, Zeiss Ultra 55, Oberkochen, Germany) and transmission electron microscope (TEM, FEI Tecnai G2 F20, College Station, TX, USA). The phase composition of the electrodes was analyzed by X-ray diffractometry (XRD, Panalytical X'Pert PRO, Eindhoven, The Netherlands) with a 2θ angle range of 10–95° for Cu-kα radiation ($\lambda = 1.54056 \text{ \AA}$). The static contact angle of the electrode surface was tested using a research contact angle tester (Krüss DSA30, Hamburg, Germany) for the analysis of the hydrophilic/hydrophobic nature of the electrode surface.

2.3. Electrochemical Testing

All electrochemical tests were carried out from cells based on the standard CR2032 battery cases and purchased zinc foil (Tianjin EVS Chemical Technology Co., Ltd., Tianjin, China) with a thickness of 0.1 mm. All operations and tests were carried out at room temperature.

2.3.1. Electrochemical Tests for Symmetric Cells

Two identical bare Zn, Ag@Zn, Cu@Zn, or Ag-Cu@Zn foils were employed as the cathode and anode with glass fiber as the separator, and an aqueous ZnSO₄ solution with a concentration of 2 M as the electrolyte. The components were assembled in CR2032 coin cells. The galvanostatic charging-discharging (GCD) cycling of all symmetric batteries was performed at current densities of 0.125 mA cm⁻², 0.25 mA cm⁻², and 0.5 mA cm⁻², and plating capacities of 0.125 mA h cm⁻², 0.25 mA h cm⁻², and 0.5 mA h cm⁻². The electrochemical corrosion resistance of the symmetrical cells was tested on an electrochemical workstation (CHI660E) within a voltage range of −0.25–0.5 V. The electrochemical impedance spectrum (EIS) was captured in the frequency range of 10⁵ Hz–10^{−1} Hz on the CHI660E.

2.3.2. Electrochemical Testing for Zn | MnO₂ Full Batteries

The impact of different anodes of Ag@Zn, Cu@Zn, and Ag-Cu@Zn anodes on the performance of full batteries was investigated. Commercial MnO₂ was used as the cathode in the full batteries. The SEM of commercial MnO₂ is shown in Figure S2a. MnO₂, acetylene

black, and polyvinylidene fluoride (PVDF) binding agent were weighed in a ratio of 7:2:1 and uniformly homogenized in N-methyl pyrrolidone (NMP) solvent before the resulting paste was coated on a stainless-steel mesh. The cathode was obtained after drying at 105 °C. A solution of 2 M ZnSO₄ and 0.1 M MnSO₄, serving as the electrolyte, along with a glass fiber separator, was employed to assemble the CR2032 coin cell. The battery's long-term performance testing was conducted using the Neware battery test system operating at a 1 C rate within a voltage range of 0.8–1.8 V. Additionally, cyclic voltammetry (CV) tests were performed at a scan rate of 0.5 mV s⁻¹, using the same voltage range, on the CHI660E electrochemical workstation.

3. Results and Discussion

The Ag-Cu@Zn anode material is characterized by X-ray diffraction (XRD) to determine its phase composition (Figure 2a). The diffraction peaks of the sample match the standard diffraction patterns of Ag, Cu, and Zn. This confirms that Ag and Cu are successfully deposited on the Zn foil. The surface morphology of the zinc foil disc and Ag-Cu@Zn anodes is shown in the scanning electron microscope (SEM) image in Figures 2b,d, and S1a,b. During the bimetal coating process, the color of the initial pure metallic zinc foil (illustration in Figure S1a) changes from silvery white with a distinct metallic luster to dark brown. As the reaction continues, the foil eventually turns black (illustration in Figure 2d). Figure 2d shows that the Ag-Cu@Zn anode surface is covered by a flat layer of material, which might be the abundant Ag and Cu particles adhering to the zinc foil disc surface. The high magnification SEM in Figure 2b shows a uniform mixture in the form of needles and granules on the surface of the Ag-Cu@Zn anode. The EDS mapping images (illustrated in Figure 2c,e,f) show that silver, copper, and zinc elements are evenly distributed on the Ag-Cu@Zn anode surface. From TEM images shown in Figure 2g,h, lattice spacings of 0.209 nm, 0.234 nm, and 0.247 nm are identified, corresponding to the (111) plane of Cu, the (111) plane Ag, and the (002) planes of Zn, respectively. Contact angle measurements were performed on the Ag-Cu@Zn and the bare zinc electrode. As shown in Figure S1c, the wettability of the Ag-Cu@Zn anode was altered after the surface modification as indicated by a contact angle of 138°, which suggests a higher level of hydrophobicity compared to the bare zinc anode which has a contact angle of 108°. Enhanced hydrophobicity diminishes the electrolyte-electrode contact, thereby facilitating the suppression of undesired side reactions.

To analyze the influence of the modified layer on Zn plating/stripping, electrochemical tests are carried out on symmetrical and full batteries equipped with bare Zn anodes and Ag-Cu@Zn anodes. Firstly, the Zn || ZnSO₄ || Zn and Ag-Cu@Zn || ZnSO₄ || Ag-Cu@Zn symmetric batteries are assembled to assess their long-term cycling stability. The cycling performance of the symmetrical cells is investigated at current densities of 0.125 mA cm⁻², 0.25 mA cm⁻², and 0.5 mA cm⁻². As shown in the GCD curve in Figure 3a, the Ag-Cu@Zn anode can reduce the polarization voltage compared to the bare zinc symmetric battery. The voltage hysteresis of the Ag-Cu@Zn symmetrical cell is 0.0511 V after 200 h cycling, which is lower than that of 0.0604 V from the bare Zn symmetrical cell (Figure S3a). Even when the current density increases to 0.5 mA cm⁻², the voltage hysteresis of the Ag-Cu@Zn symmetrical cell is only 0.0505 V, whereas the voltage hysteresis of the bare Zn symmetrical cell increases to 0.0765 V (Figure S3b). The nucleation overpotential (NOP) during deposition can be determined by examining a magnified portion of the initial phase of the GCD curves (Figure S2b). As the first charge process progresses, the bare zinc symmetric battery exhibits a high initial nucleation potential of 143 mV, which decreases to 30 mV as the first charge process ends, therefore the NOP is 113 mV. On the other hand, the Ag-Cu@Zn anode reduces the initial nucleation potential for zinc deposition to 69 mV and it further decreases to 44 mV by the end of the first charge process. Based on this, it can be inferred that the overpotential (NOP) of the Ag-Cu@Zn symmetric battery is only 25 mV. This indicates that the introduction of Ag and Cu metals can significantly reduce the nucleation overpotential and promote a more homogeneous zinc deposition/exfoliation

process. This is explained by the fact that Ag and Cu have decent room temperature solubility in Zn. As a result, a solid solution buffer layer with a hcp (hexagonal close-packed) structure similar to that of zinc was formed, greatly aiding the nucleation process [32]. As shown in Figure 3b, at current densities of 0.125 mA cm^{-2} the bare Zn symmetrical battery has a voltage instability at 690 h and became short cut at 717 h. This is essentially a short-circuit fault caused by internal dendrite growth piercing the diaphragm. With the increase in current density, short circuits occur faster [22]. The Ag-Cu@Zn symmetrical battery, under the same charge and discharge conditions, has a relatively longer and more stable cycle life. The EIS of symmetrical cells based on different metal overlays was performed before and after the first cycle in 2 M ZnSO_4 aqueous electrolyte, to investigate their impact on reaction kinetics. By fitting the equivalent circuit in Figure S6, the results are shown in Figure 3c,d. The semicircle in the Nyquist plot is linked to the transfer resistance R_{ct} . The bare Zn symmetric battery in the plot shows large charge transfer resistances of $0.95 \text{ k}\Omega$ and $0.44 \text{ k}\Omega$. The Cu@Zn symmetric battery shows $R_{ct} = 0.69 \text{ k}\Omega$ of the original transfer resistance and it reduces to $0.28 \text{ k}\Omega$ after the first cycle. The Ag-Cu@Zn symmetric battery shows even smaller resistance values of $0.22 \text{ k}\Omega$ before the first cycle and $0.12 \text{ k}\Omega$ after cycling. The smallest transfer resistance R_{ct} is observed in the Ag@Zn symmetric battery, which is $0.20 \text{ k}\Omega$ and turns to $0.05 \text{ k}\Omega$ after cycling. It is conspicuous that the involvement of Ag considerably reduces the charge transfer impedance. This stems from its extraordinary compatibility with Zn and the low lattice distortion during Zn plating and stripping, compared with other metals [33]. In alignment with the findings from EIS testing in Figure 3c,d, the Ag-Cu@Zn and Ag@Zn electrode delivered the desired rate performance with reduced overpotential compared to Cu-Zn and Zn electrodes at all current densities applied as a result of the positive contribution from adding Ag (Figure 3e). The performance of the Ag-Cu@Zn symmetric cell was compared with other research studies (as shown in Table S1 [34–42] in the supplementary materials), revealing a significant reduction in nucleation overpotential and a favorable cycle time compared to the other works.

As shown in the cross-section SEM images of the Ag-Cu@Zn anode before cycling (Figure 4a), the thickness of the bimetal modulated layer is about $10 \mu\text{m}$. The EDS mappings (Figure 4b) of the cross-section in the modified anode show that Ag and Cu elements are evenly distributed, further confirming the formation of the modification layer. The XRD patterns in Figure 4c present the alloy phases of AgZn_5 and CuZn_5 alloys in the Ag-Cu@Zn anode after 100 cycles. But it is not visible in the XRD patterns of the Ag-Cu@Zn anode before cycling, which shows that the alloys are gradually formed during the charge/discharge process. This aligns with the principles of thermodynamics in alloy creation, where the alloying process results in negative Gibbs free energy change [43]. The alloying process can effectively reduce the nucleation overpotential of Zn^{2+} , induce its uniform deposition, improve the affinity between the anode and Zn, and reduce the interfacial charge transfer impedance [25].

To examine the effect of the alloy overlays on ZIBs, full batteries with both bare Zn and Ag-Cu@Zn anodes are evaluated at various electrochemical conditions. Figure 4d–f and Figure 4g–i show the SEM images of the two systems after 1, 5, and 10 cycles that are run at the current density of 0.3 A g^{-1} , respectively. After the first cycle, the bare zinc anode has uneven nucleation on the surface, and the surface is covered with zinc clusters that have built up after deposition after the subsequent 5 cycles. After 10 cycles, the zinc clusters developed into bumps and protrusions of uneven sizes, which further provokes the tip effect and exacerbates the situation of dendrite formation. In contrast, the surface of the Ag-Cu@Zn anode gradually becomes compact in 1–5 cycles, and the gaps on the surface of the alloy layer are continuously filled by laterally growing Zn in 10 cycles. From the magnified view of selected sections from the XRD pattern (Figure S4), it can be concluded that the in situ formed AgZn_3 alloy preferentially exposes the (002) plane which has been proven beneficial to the epitaxial seeded growth of Zn [44]. Consequently, the notorious propensity for Zn to be rapidly deposited on (100) and (101) planes, which leads to the unfortunate flaky dendrites, is inhibited. Meanwhile, by capitalizing on the strong binding capability of CuZn_5 with Zn [45], intense anchoring of freshly deposited

Zn atoms could be realized. This appreciably hampers the otherwise active diffusion of Zn in vertical directions, hence further restricting dendrite formation (the schematic is shown in Figure 5a).

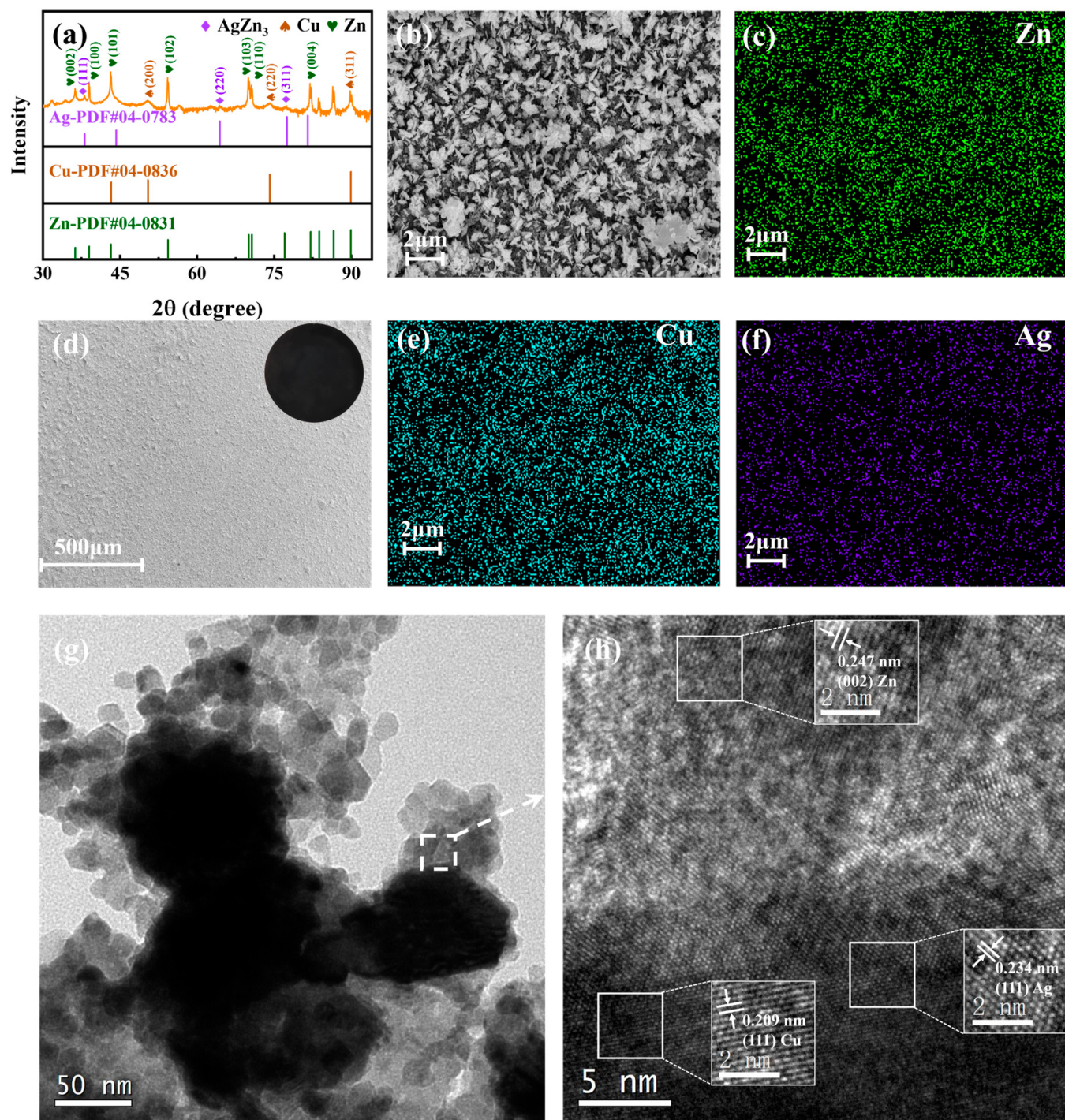


Figure 2. (a) the XRD pattern of the Ag-Cu@Zn anode before electrochemical cycling; SEM images (b,d) and EDS mapping (c,e,f) of the Ag-Cu@Zn anode; and (g,h) TEM and the corresponding high-resolution transmission electron microscopy (HRTEM) images of Ag-Cu@Zn (the arrow points to the HRTEM analysis of the box region in Figure 2g).

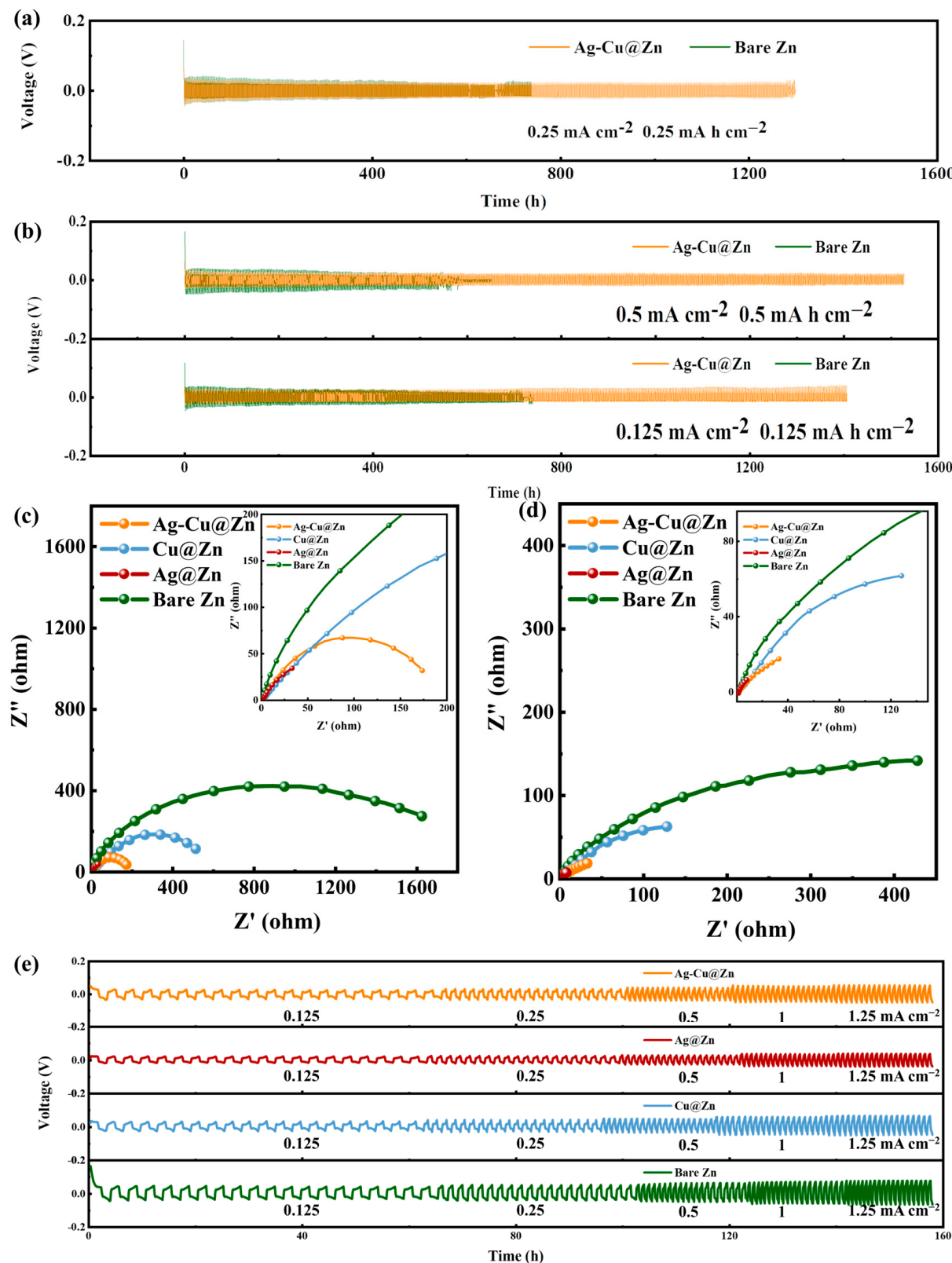


Figure 3. (a) Comparison in GCD curve between the bare Zn and Ag-Cu@Zn symmetrical cells at 0.25 mA cm^{-2} for $0.25 \text{ mA h cm}^{-2}$. (b) GCD curves of cells based on Zn and Ag-Cu@Zn, measured at 0.125 mA cm^{-2} for $0.125 \text{ mA h cm}^{-2}$ and 0.5 mA cm^{-2} for 0.5 mA h cm^{-2} ; electrochemical impedance spectra (EIS) of symmetrical cells based on various anodes (c) before and (d) after the first cycle; and (e) comparison in rate capability of symmetric cells assembled from different anodes at current densities in the range of 0.125 to 1.25 mA cm^{-2} .

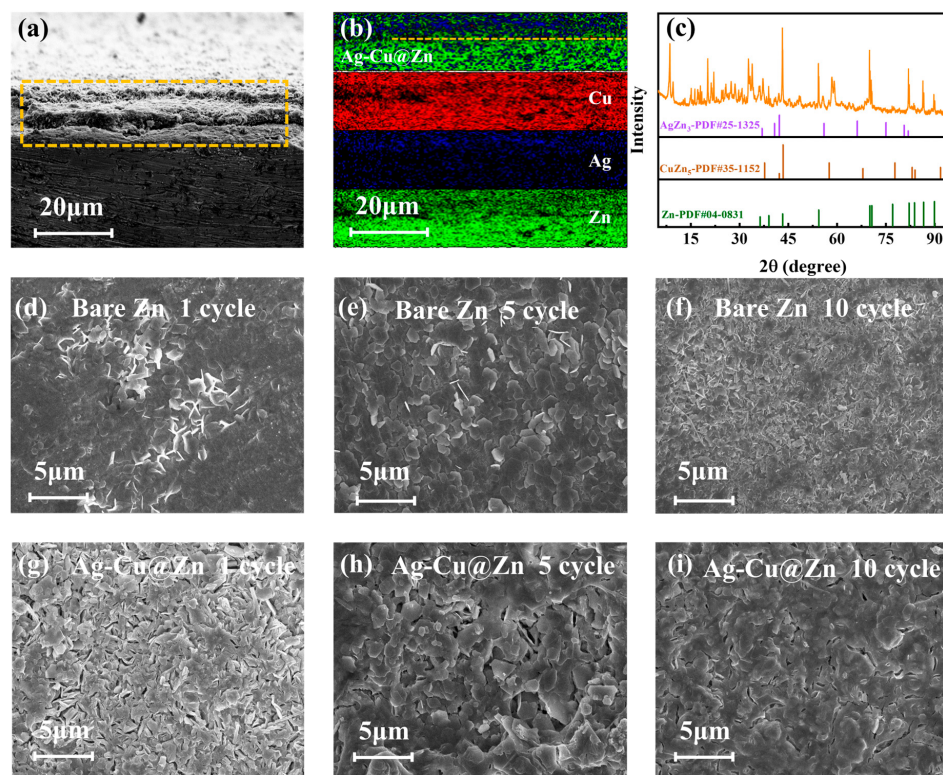


Figure 4. The cross-section SEM (a) and EDS (b) image of Ag-Cu@Zn anode; (c) the XRD pattern of the Ag-Cu@Zn anode after 100 cycles; SEM images of the bare Zn anode (d–f) and the Ag-Cu@Zn anode (g–i) after 1, 5, and 10 cycles at the current density of 0.3 A g^{-1} .

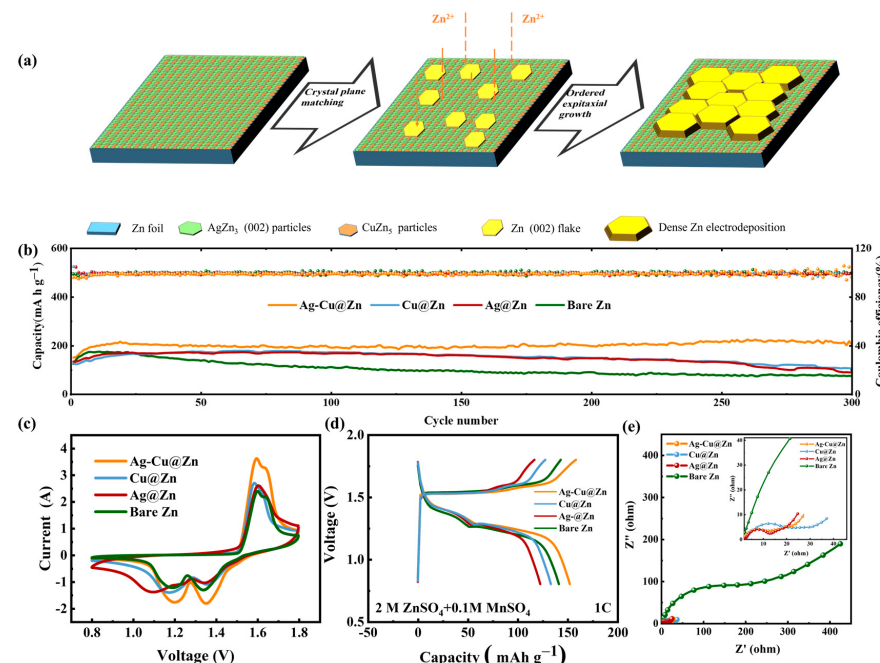


Figure 5. (a) a schematic diagram for the dendrite-free Zn deposition resulting from the synergistic regulation by AgZn_3 and CuZn_5 particles on Ag-Cu@Zn; (b) the long-term cycling stability test on full batteries assembled from various anodes at 1C; CV curves measured at the scan rate of 0.5 mV s^{-1} (c,d) the fifth cycle charge–discharge curves obtained at 1C of full batteries assembled from various anodes; (e) and EIS of all full batteries.

It is believed that these two processes can be mutually enhanced in a concerted manner, synergistically boosting the stability of the reactive interface. To examine this, the cycling stability and coulombic efficiency (CE) of four Zn-MnO₂ batteries based on bare Zn, Ag@Zn, Cu@Zn, Ag-Cu@Zn anodes are tested in Figure 5b. At a rate of 1 C (1 C = 308 mA g⁻¹), the capacity gradually increases from an initial 150 mA h g⁻¹ to 216 mA h g⁻¹ in the Ag-Cu@Zn electrode and maintains at 217 mA h g⁻¹ after 300 cycles. On the other hand, the bare zinc full battery only delivers an initial capacity of 124 mA h g⁻¹ at the same rate, and 172 mA h g⁻¹ is obtained after the 20 cycles. The capacity decreases rapidly in the subsequent cycles with only 75 mA h g⁻¹ retained after 300 cycles. Though the Ag@Zn || MnO₂ full battery and the Cu@Zn || MnO₂ full battery show improved cycling performance than the bare Zn, they both exhibit rapid decay after 100 cycles with 83% and 65% capacity retained, respectively. The conspicuously improved cycling stability in the bimetallic system undoubtedly validates the synergy between the Zn regulation process controlled by AgZn₃ and CuZn₅ alloys as exhibited in Figure 5b. From the CV curves shown in Figure 5c, redox peaks at 1.196/1.642 V and 1.352/1.596 V can be identified for the Ag-Cu@Zn || MnO₂ full battery, which can be attributed to the Zn²⁺ insertion into and extraction from MnO₂. According to the CV curve, the |ΔE_p| of the Zn || MnO₂ (0.284 V) and Cu@Zn || MnO₂ (0.283 V) are very close. Yet, the other two are lower (Ag@Zn || MnO₂ (0.229 V) and Ag-Cu@Zn || MnO₂ (0.234 V)). The lower |ΔE_p| indicates less polarization, better reversibility, and faster reaction kinetics, which is also consistent with findings from the EIS measurement on full batteries as shown in (Figure 5e) and those from Figure 3b,c. In addition, Ag-Cu@Zn || MnO₂ delivers the highest gravimetric capacity as demonstrated in the charge-discharge curve in Figure 5d at the rate of 1 C. The increased capacity observed in the bimetallic anode could be attributed to the increased exposure of reaction sites resulting from the higher corrosion resistance and inhibited side reactions. Linear polarization measurement was performed to investigate the anti-corrosion performance (Figure S5). The Ag-Zn@Zn electrode exhibits the lowest corrosion current and the most positive corrosion potential which is affected by the higher redox potential of Cu²⁺/Cu and Ag⁺/Ag as compared to that of Zn²⁺/Zn. The result signifies an enhanced anti-corrosion behavior. By leveraging the synergistic effects of different metals and utilizing their individual strengths, outstanding performance was achieved. This was especially evident in the cycling stability, which favorably compares with other Zn ion aqueous batteries using a MnO₂ cathode, as demonstrated in Table S2 [23,35–37,40,46–48] in the supplementary materials.

4. Conclusions

Through a simple heterogeneous interface substitution reaction involving the oxidants of Ag⁺ and Cu²⁺, Zn anode overlaid with uniform protective bimetals has been realized. The approach explores the possibility of creating synergy between AgZn₃ and CuZn₅ alloys to coordinate the regulation of Zn deposition in a dendrite-free manner for ZIB with outstanding stability. Previously unexplored, the field of multi-metal alloying has been delved into with this work, filling a significant gap in the literature. Additionally, the mechanism underlying multi-metal synergy is examined and proposed. It is anticipated that the insights from this work could have an impact on the advancement of next-generation multicomponent high performance ZIBs.

Supplementary Materials: The following supporting information can be downloaded at: <https://www.mdpi.com/article/10.3390/batteries10030070/s1>, Figure S1: (a,b) SEM of the bare zinc anode, (c) Contact angle test of Bare Zn and Ag-Cu@Zn electrodes with water. Figure S2: (a)The SEM image of the commercial MnO₂, (b) Voltage profiles for the initial Zn nucleation at 0.25 mA cm⁻². Figure S3: Detailed voltage profiles of bare Zn and Ag-Cu@Zn symmetric cells after cycling 200 h at 0.25 mA cm⁻² (a) and 0.5 mA cm⁻² (b), respectively. Figure S4: The magnified view of selected sections from the XRD pattern. Figure S5: Linear polarization curve of the brae Zn, Ag@Zn, Cu@Zn, and Ag-Cu@Zn anodes. Figure S6: The equivalent circuit for fitting the EIS of the symmetric cells. R1 denotes the equivalent serial resistance, R2 denotes the charge transfer resistance, W represents the

Warburg resistance, and CPE stands for “Constant phase element”. Table S1: Comparison with the Ag-Cu@Zn symmetrical cell and other symmetrical cells with different protective layers on Zn foil disc. Table S2: Comparison with MnO₂-based batteries with other alloy-modified Zn anodes and some Zn anodes with other types of protective coatings.

Author Contributions: Conceptualization, Y.L. and F.Y.; data curation, M.L.; formal analysis, H.Y.; methodology, H.Y. and Y.Z.; project administration, G.X.; resources, G.X. and W.K.; supervision, G.X.; writing—original draft, H.Y.; writing—review and editing, W.K. All authors have read and agreed to the published version of the manuscript.

Funding: This work is supported by the Longshan academic talent research supporting program of SWUST (No. 22zx7102) and the key scientific research projects of the Southwest University of Science and Technology (No. 17zx910201).

Data Availability Statement: The data are not publicly available due to privacy.

Acknowledgments: The authors would like to thank the support of the State Key Laboratory of Environmentally Friendly Energy Materials. The authors would also like to thank the reviewers for their constructive suggestions that helped improve the quality of this manuscript.

Conflicts of Interest: The authors declare no conflicts of interest.

References

1. Bennear, L.S. Energy Justice, Decarbonization, and the Clean Energy Transformation. *Annu. Rev. Resour. Econ.* **2022**, *14*, 647–668. [[CrossRef](#)]
2. Carley, S.; Konisky, D.M. The justice and equity implications of the clean energy transition. *Nat. Energy* **2020**, *5*, 569–577. [[CrossRef](#)]
3. Davidson, D.J. Exnovating for a renewable energy transition. *Nat. Energy* **2019**, *4*, 254–256. [[CrossRef](#)]
4. Han, C.; Li, W.; Liu, H.K.; Dou, S.; Wang, J. Principles and strategies for constructing a highly reversible zinc metal anode in aqueous batteries. *Nano Energy* **2020**, *74*, 104880. [[CrossRef](#)]
5. Mainar, A.R.; Iruin, E.; Colmenares, L.C.; Kvasha, A.; de Meatza, I.; Bengoechea, M.; Leonet, O.; Boyano, I.; Zhang, Z.; Blazquez, J.A. An overview of progress in electrolytes for secondary zinc-air batteries and other storage systems based on zinc. *J. Energy Storage* **2018**, *15*, 304–328. [[CrossRef](#)]
6. Brockway, P.E.; Owen, A.; Brand-Correa, L.I.; Hardt, L. Estimation of global final-stage energy-return-on-investment for fossil fuels with comparison to renewable energy sources. *Nat. Energy* **2019**, *4*, 612–621. [[CrossRef](#)]
7. Kittner, N.; Lill, F.; Kammen, D.M. Energy storage deployment and innovation for the clean energy transition. *Nat. Energy* **2017**, *2*, 17125. [[CrossRef](#)]
8. Turner, J.M. The matter of a clean energy future. *Science* **2022**, *376*, 1361. [[CrossRef](#)]
9. Liu, H.; Zhou, Q.; Xia, Q.; Lei, Y.; Huang, X.L.; Tebyetekerwa, M.; Zhao, X.S. Interface challenges and optimization strategies for aqueous zinc-ion batteries. *J. Energy Chem.* **2023**, *77*, 642–659. [[CrossRef](#)]
10. Shang, Y.; Kundu, D. Understanding and Performance of the Zinc Anode Cycling in Aqueous Zinc-Ion Batteries and a Roadmap for the Future. *Batter. Supercaps* **2022**, *5*, e202100394. [[CrossRef](#)]
11. Wang, T.; Sun, J.; Hua, Y.; Krishna, B.N.V.; Xi, Q.; Ai, W.; Yu, J.S. Planar and dendrite-free zinc deposition enabled by exposed crystal plane optimization of zinc anode. *Energy Storage Mater.* **2022**, *53*, 273–304. [[CrossRef](#)]
12. Zuo, Y.; Wang, K.; Pei, P.; Wei, M.; Liu, X.; Xiao, Y.; Zhang, P. Zinc dendrite growth and inhibition strategies. *Mater. Today Energy* **2021**, *20*, 100692. [[CrossRef](#)]
13. Mainar, A.R.; Colmenares, L.C.; Blázquez, J.A.; Urdampilleta, I. A brief overview of secondary zinc anode development: The key of improving zinc-based energy storage systems. *Int. J. Energy Res.* **2018**, *42*, 903–918. [[CrossRef](#)]
14. Mohammadi, A.; Hagopian, A.; Sayegh, S.; Bechelany, M.; Filhol, J.-S.; Younesi, R.; Stievano, L.; Monconduit, L. Towards understanding the nucleation and growth mechanism of Li dendrites on zinc oxide-coated nickel electrodes. *J. Mater. Chem. A* **2022**, *10*, 17593–17602. [[CrossRef](#)]
15. Deng, Q.; Liu, F.; Wu, X.; Li, C.; Zhou, W.; Long, B. An aqueous BiI₃-Zn battery with dual mechanisms of Zn²⁺ (de)intercalation and I⁻/I₂ redox. *J. Energy Chem.* **2024**, *89*, 670–678. [[CrossRef](#)]
16. Li, Y.; Yang, S.; Du, H.; Liu, Y.; Wu, X.; Yin, C.; Wang, D.; Wu, X.; He, Z.; Wu, X. A stable fluoride-based interphase for a long cycle Zn metal anode in an aqueous zinc ion battery. *J. Mater. Chem. A* **2022**, *10*, 14399–14410. [[CrossRef](#)]
17. Lin, H.; Zhang, Q.; Liu, H.; Shen, S.; Guo, Z.; Jin, B.; Peng, R. Understanding the synergistically enhanced thermocatalytic decomposition of ammonium perchlorate using cobalt nanoparticle-embedded nitrogen-doped graphitized carbon. *Mater. Adv.* **2023**, *4*, 2332–2339. [[CrossRef](#)]
18. Qian, Y.; Wang, H.; Li, X.; Song, T.; Pei, Y.; Liu, L.; Long, B.; Wu, X.; Wang, X. Sn-doped BiOCl nanosheet with synergistic H⁺/Zn²⁺ co-insertion for “rocking chair” zinc-ion battery. *J. Energy Chem.* **2023**, *81*, 623–632. [[CrossRef](#)]
19. Wang, S.J.; Yang, Z.; Chen, B.T.; Zhou, H.; Wan, S.F.; Hu, L.Z.; Qiu, M.; Qie, L.; Yu, Y. A highly reversible, dendrite-free zinc metal anodes enabled by a dual-layered interface. *Energy Storage Mater.* **2022**, *47*, 491–499. [[CrossRef](#)]

20. Li, Z.; Wang, H.; Zhong, Y.; Yuan, L.; Huang, Y.; Li, Z. Highly Reversible and Anticorrosive Zn Anode Enabled by a Ag Nanowires Layer. *ACS Appl. Mater. Interfaces* **2022**, *14*, 9097–9105. [CrossRef] [PubMed]
21. Wang, N.; Wan, H.; Duan, J.; Wang, X.; Tao, L.; Zhang, J.; Wang, H. A review of zinc-based battery from alkaline to acid. *Mater. Today Adv.* **2021**, *11*, 100149. [CrossRef]
22. Yang, Q.; Li, Q.; Liu, Z.; Wang, D.; Guo, Y.; Li, X.; Tang, Y.; Li, H.; Dong, B.; Zhi, C. Dendrites in Zn-Based Batteries. *Adv. Mater.* **2020**, *32*, e2001854. [CrossRef]
23. Zhang, Y.; Peng, C.; Zhang, Y.; Yang, S.; Zeng, Z.; Zhang, X.; Qie, L.; Zhang, L.-L.; Wang, Z. In-situ crosslinked Zn^{2+} -conducting polymer complex interphase with synergistic anion shielding and cation regulation for high-rate and dendrite-free zinc metal anodes. *Chem. Eng. J.* **2022**, *448*, 137653. [CrossRef]
24. Wei, X.; Desai, D.; Yadav, G.G.; Turney, D.E.; Couzis, A.; Banerjee, S. Impact of anode substrates on electrodeposited zinc over cycling in zinc-anode rechargeable alkaline batteries. *Electrochim. Acta* **2016**, *212*, 603–613. [CrossRef]
25. Li, H.; Jia, W.; Chen, P.; Wang, L.; Yan, X.; Yang, Y.-Y. Zinc deposition characteristics on different substrates for aqueous zinc ion battery. *Appl. Surf. Sci.* **2023**, *607*, 155111. [CrossRef]
26. Cai, Z.; Ou, Y.; Wang, J.; Xiao, R.; Fu, L.; Yuan, Z.; Zhan, R.; Sun, Y. Chemically resistant Cu-Zn/Zn composite anode for long cycling aqueous batteries. *Energy Storage Mater.* **2020**, *27*, 205–211. [CrossRef]
27. Zhang, Y.; Wang, G.; Yu, F.; Xu, G.; Li, Z.; Zhu, M.; Yue, Z.; Wu, M.; Liu, H.-K.; Dou, S.-X.; et al. Highly reversible and dendrite-free Zn electrodeposition enabled by a thin metallic interfacial layer in aqueous batteries. *Chem. Eng. J.* **2021**, *416*, 128062. [CrossRef]
28. Wang, Y.; Chen, Y.; Liu, W.; Ni, X.; Qing, P.; Zhao, Q.; Wei, W.; Ji, X.; Ma, J.; Chen, L. Uniform and dendrite-free zinc deposition enabled by in situ formed AgZn₃ for the zinc metal anode. *J. Mater. Chem. A* **2021**, *9*, 8452–8461. [CrossRef]
29. Cao, P.; Tang, J.; Wei, A.; Bai, Q.; Meng, Q.; Fan, S.; Ye, H.; Zhou, Y.; Zhou, X.; Yang, J. Manipulating Uniform Nucleation to Achieve Dendrite-Free Zn Anodes for Aqueous Zn-Ion Batteries. *ACS Appl. Mater. Interfaces* **2021**, *13*, 48855–48864. [CrossRef]
30. Peng, Y.; Lai, C.; Zhang, M.; Liu, X.; Yin, Y.; Li, Y.; Wu, Z. Zn-Sn alloy anode with repressible dendrite grown and meliorative corrosion resistance for Zn-air battery. *J. Power Sources* **2022**, *526*, 231173. [CrossRef]
31. Zhang, Q.; Liu, D.; Zhang, Y.; Guo, Z.; Chen, M.; Chen, Y.; Jin, B.; Song, Y.; Pan, H. Insight into coupled Ni-Co dual-metal atom catalysts for efficient synergistic electrochemical CO₂ reduction. *J. Energy Chem.* **2023**, *87*, 509–517. [CrossRef]
32. Zhang, Y.; Howe, J.D.; Ben-Yoseph, S.; Wu, Y.; Liu, N. Unveiling the Origin of Alloy-Seeded and Nondendritic Growth of Zn for Rechargeable Aqueous Zn Batteries. *ACS Energy Lett.* **2021**, *6*, 404–412. [CrossRef]
33. Li, B.; Yang, K.; Ma, J.; Shi, P.; Chen, L.; Chen, C.; Hong, X.; Cheng, X.; Tang, M.C.; He, Y.B.; et al. Multicomponent Copper-Zinc Alloy Layer Enabling Ultra-Stable Zinc Metal Anode of Aqueous Zn-ion Battery. *Angew. Chem. Int. Ed. Engl.* **2022**, *61*, e202212587. [CrossRef]
34. Guo, W.; Zhang, Y.; Tong, X.; Wang, X.; Zhang, L.; Xia, X.; Tu, J. Multifunctional tin layer enabled long-life and stable anode for aqueous zinc-ion batteries. *Mater. Today Energy* **2021**, *20*, 100675. [CrossRef]
35. Yang, Z.; Lv, C.; Li, W.; Wu, T.; Zhang, Q.; Tang, Y.; Shao, M.; Wang, H. Revealing the Two-Dimensional Surface Diffusion Mechanism for Zinc Dendrite Formation on Zinc Anode. *Small* **2022**, *18*, e2104148. [CrossRef] [PubMed]
36. Zou, P.; Nykypanchuk, D.; Doerk, G.; Xin, H.L. Hydrophobic Molecule Monolayer Brush-Tethered Zinc Anodes for Aqueous Zinc Batteries. *ACS Appl. Mater. Interfaces* **2021**, *13*, 60092–60098. [CrossRef] [PubMed]
37. Bao, Q.-P.; Sui, B.-B.; Wang, P.-F.; Gong, Z.; Zhang, Y.-H.; Wu, Y.-H.; Zhao, L.-N.; Tang, J.-J.; Zhou, M.-D.; Shi, F.-N. High-pressure deformation exposes zinc (002) crystal planes adapted for high-performance zinc anodes. *Electrochim. Acta* **2024**, *478*, 143824. [CrossRef]
38. Xiao, P.; Xue, L.; Guo, Y.; Hu, L.; Cui, C.; Li, H.; Zhai, T. On-site building of a Zn^{2+} -conductive interfacial layer via short-circuit energization for stable Zn anode. *Sci. Bull.* **2021**, *66*, 545–552. [CrossRef]
39. Han, D.; Wu, S.; Zhang, S.; Deng, Y.; Cui, C.; Zhang, L.; Long, Y.; Li, H.; Tao, Y.; Weng, Z.; et al. A Corrosion-Resistant and Dendrite-Free Zinc Metal Anode in Aqueous Systems. *Small* **2020**, *16*, 2001736. [CrossRef]
40. Cui, M.; Xiao, Y.; Kang, L.; Du, W.; Gao, Y.; Sun, X.; Zhou, Y.; Li, X.; Li, H.; Jiang, F.; et al. Quasi-Isolated Au Particles as Heterogeneous Seeds To Guide Uniform Zn Deposition for Aqueous Zinc-Ion Batteries. *ACS Appl. Energy Mater.* **2019**, *2*, 6490–6496. [CrossRef]
41. Lu, Q.; Liu, C.; Du, Y.; Wang, X.; Ding, L.; Omar, A.; Mikhailova, D. Uniform Zn Deposition Achieved by Ag Coating for Improved Aqueous Zinc-Ion Batteries. *ACS Appl. Mater. Interfaces* **2021**, *13*, 16869–16875. [CrossRef]
42. Qi, Z.; Xiong, T.; Yu, Z.G.; Meng, F.; Chen, B.; Xiao, H.; Xue, J. Suppressing zinc dendrite growth in aqueous battery via Zn-Al alloying with spatially confined zinc reservoirs. *J. Power Sources* **2023**, *558*, 232628. [CrossRef]
43. Qin, Y.; Li, H.; Han, C.; Mo, F.; Wang, X. Chemical Welding of the Electrode-Electrolyte Interface by Zn-Metal-Initiated In Situ Gelation for Ultralong-Life Zn-Ion Batteries. *Adv. Mater.* **2022**, *34*, e2207118. [CrossRef] [PubMed]
44. Lu, H.; Jin, Q.; Jiang, X.; Dang, Z.M.; Zhang, D.; Jin, Y. Vertical Crystal Plane Matching between AgZn₃ (002) and Zn (002) Achieving a Dendrite-Free Zinc Anode. *Small* **2022**, *18*, e2200131. [CrossRef] [PubMed]
45. Meng, H.; Ran, Q.; Dai, T.Y.; Shi, H.; Zeng, S.P.; Zhu, Y.F.; Wen, Z.; Zhang, W.; Lang, X.Y.; Zheng, W.T.; et al. Surface-Alloyed Nanoporous Zinc as Reversible and Stable Anodes for High-Performance Aqueous Zinc-Ion Battery. *Nanomicro Lett.* **2022**, *14*, 128. [CrossRef]
46. Fu, H.; Wen, Q.; Li, P.Y.; Wang, Z.Y.; He, Z.J.; Yan, C.; Mao, J.; Dai, K.H.; Zhang, X.H.; Zheng, J.C. In-situ chemical conversion film for stabilizing zinc metal anodes. *J. Energy Chem.* **2022**, *73*, 387–393. [CrossRef]

47. Wang, S.-B.; Ran, Q.; Yao, R.-Q.; Shi, H.; Wen, Z.; Zhao, M.; Lang, X.-Y.; Jiang, Q. Lamella-nanostructured eutectic zinc–aluminum alloys as reversible and dendrite-free anodes for aqueous rechargeable batteries. *Nat. Commun.* **2020**, *11*, 1634. [[CrossRef](#)]
48. Xue, R.; Kong, J.; Wu, Y.; Wang, Y.; Kong, X.; Gong, M.; Zhang, L.; Lin, X.; Wang, D. Highly reversible zinc metal anodes enabled by a three-dimensional silver host for aqueous batteries. *J. Mater. Chem. A* **2022**, *10*, 10043–10050. [[CrossRef](#)]

Disclaimer/Publisher’s Note: The statements, opinions and data contained in all publications are solely those of the individual author(s) and contributor(s) and not of MDPI and/or the editor(s). MDPI and/or the editor(s) disclaim responsibility for any injury to people or property resulting from any ideas, methods, instructions or products referred to in the content.